

AN IMAGE-PLANE ALGORITHM FOR *JWST*'S NON-REDUNDANT APERTURE MASK DATA

ALEXANDRA Z. GREENBAUM¹, LAURENT PUEYO², ANAND SIVARAMAKRISHNAN^{2,4,5}, AND SYLVESTRE LACOUR³

¹ Johns Hopkins University Department of Physics and Astronomy 3400 North Charles, Baltimore, MD 21218

² Space Telescope Science Institute, 3700 San Martin Drive, Baltimore, MD 21218

³ LESIA, CNRS/UMR-8109, Observatoire de Paris, UPMC, Université Paris Diderot 5 place Jules Janssen, 92195 Meudon, France

Received 2013 March 18; accepted 2014 November 8; published 2014 December 22

ABSTRACT

The high angular resolution technique of non-redundant masking (NRM) or aperture masking interferometry (AMI) has yielded images of faint protoplanetary companions of nearby stars from the ground. AMI on *James Webb Space Telescope* (*JWST*)'s Near Infrared Imager and Slitless Spectrograph (NIRISS) has a lower thermal background than ground-based facilities and does not suffer from atmospheric instability. NIRISS AMI images are likely to have 90%–95% Strehl ratio between 2.77 and 4.8 μm . In this paper we quantify factors that limit the raw point source contrast of *JWST* NRM. We develop an analytic model of the NRM point spread function which includes different optical path delays (pistons) between mask holes and fit the model parameters with image plane data. It enables a straightforward way to exclude bad pixels, is suited to limited fields of view, and can incorporate effects such as intra-pixel sensitivity variations. We simulate various sources of noise to estimate their effect on the standard deviation of closure phase, σ_{CP} (a proxy for binary point source contrast). If $\sigma_{\text{CP}} < 10^{-4}$ radians—a contrast ratio of 10 mag—young accreting gas giant planets (e.g., in the nearby Taurus star-forming region) could be imaged with *JWST* NIRISS. We show the feasibility of using NIRISS' NRM with the sub-Nyquist sampled F277W, which would enable some exoplanet chemistry characterization. In the presence of small piston errors, the dominant sources of closure phase error (depending on pixel sampling, and filter bandwidth) are flat field errors and unmodeled variations in intra-pixel sensitivity. The in-flight stability of NIRISS will determine how well these errors can be calibrated by observing a point source. Our results help develop efficient observing strategies for space-based NRM.

Key words: instrumentation: interferometers – planetary systems – space vehicles: instruments – techniques: high angular resolution

1. INTRODUCTION

Recent direct detections of exoplanets open a spectroscopic window into the atmosphere and physics of young and adolescent exoplanets. They are an important component for piecing together a complete picture of exoplanetary formation and evolution, and are complementary to indirect detections methods. Young and nearby stars have already been surveyed from a few Astronomical Units of physical separation outwards with direct imaging and coronagraphs on eight meter class telescopes (Wahhaj et al. 2013; Nielsen et al. 2013; Biller et al. 2013; Vigan et al. 2012) and are being surveyed at even higher contrast with current (Oppenheimer et al. 2012; Macintosh et al. 2012; Beuzit et al. 2008; Martinache & Guyon 2009) instrument surveys utilizing extreme adaptive optics (ExAO). However, the close environs of young systems in stellar formation regions are only accessible to ExAO systems using interferometric techniques such as non-redundant mask (NRM) interferometry (Lacour et al. 2011; Kraus & Ireland 2012; Cieza et al. 2013; Huélamo et al. 2011). NRM imaging is fundamentally limited by photon noise, so it yields moderate contrast. By comparison, coronagraphs (which suppress light from the bright central object) are capable of delivering higher contrast than NRM, but their search area does not reach as close in as that of NRM. The two techniques are complementary.

NRM was first used to improve the angular resolution of filled-aperture telescopes (Baldwin et al. 1986; Haniff et al.

1987; Tuthill et al. 2000). Its improved dynamic range helped to probe the physics of binaries at moderate contrast ratios (Lloyd et al. 2006; Ireland et al. 2008; Bernat et al. 2010; Martinache et al. 2007, 2009). More recently, NRM observations of star forming regions have discovered structures associated with the birth of exoplanets (Kraus & Ireland 2012; Cieza et al. 2013; Huélamo et al. 2011). Routine ground contrast ratio limits for NRM are 10^2 – 10^3 with the deepest contrast being $\Delta L' = 7.99$ (Hinkley et al. 2011). Today instruments combine NRM with ExAO systems (Sivaramakrishnan et al. 2010b; Zimmerman 2011; Zimmerman et al. 2012). These facilities, together with wide bandpass polarization or integral field unit spectroscopy (IFS) in the *YJHK* bands on the 8 m Gemini South telescope (Macintosh et al. 2014) as well as 2.5–5 μm NRM on the 40K *James Webb Space Telescope*'s Near Infrared Imager and Slitless Spectrograph (*JWST* NIRISS; Doyon et al. 2012; Sivaramakrishnan et al. 2010b, 2012; Greenbaum et al. 2013a), promise to extend planet formation science by enabling deeper dust penetration at longer wavelengths. These new systems will enable detection of very young (e.g., Taurus–Auriga star forming region), possibly accreting gas giant planets at small separations accessible to NIRISS NRM (Beichman et al. 2010).

In spite of the wealth of recent observational results from NRM, the literature does not include extensive discussion of the fundamental and practical limits associated with the technique. Lacour et al. (2011) discussed empirical sensitivity limits of Very Large Telescope (VLT) NACO Sparse Aperture Masking (SAM), based on experiments with the image plane fitting routine that we study here. Martinache (2010) showed how NRM can be generalized to full aperture imaging in the high Strehl ratio regime. Ireland (2013) discussed some of the

⁴ Astrophysics Department, American Museum of Natural History, 79th Street and Central Park West, New York, NY 10024, USA.

⁵ Department of Physics and Astronomy, Stony Brook University, Stony Brook, NY 11794, USA.

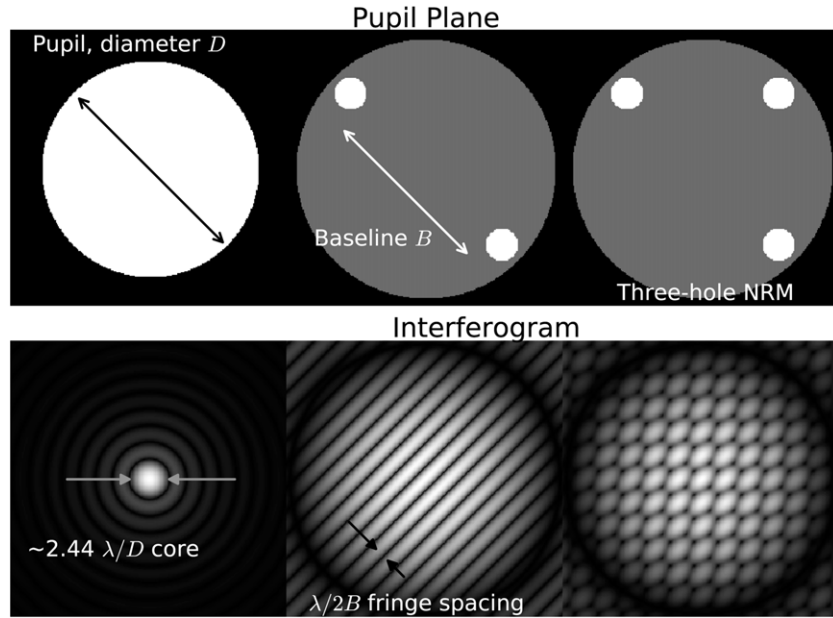


Figure 1. Pupil masks and their interferograms. Small holes produce a large PSF envelope, fringed by interference through multiple holes. The longest baselines provides finer resolution than a full aperture. The three hole pupil at right can provide a *closure phase* measurement of a celestial object.

limiting factors of high contrast NRM observations, and Hinkley et al. (2011) conducted deep NRM observations of the known multiple planetary system HR 8799.

The purpose of this paper is two-fold. First, we continue the development of the image plane approach to analyzing NRM data. We address field of view, pixel sampling, plate scale and pupil magnification stability, and some detector properties. We show that this method typically confirms the photon noise and flat field accuracy limits presented by Ireland (2013). In addition, we study other factors that limit NRM contrast—requirements on the spectral type match between a target and its calibrator star, and the effect a finite spectral bandpass has on closure phase errors. Second, we highlight factors that limit *JWST* NIRISS NRM, which fields a seven-hole NRM (Sivaramakrishnan et al. 2012). NIRISS has the best pupil image quality of all the *JWST* instruments (Bos et al. 2008), which makes it *JWST*’s best-suited instrument for aperture masking interferometry. In addition, NIRISS’s homogenous aluminum bench and optics should help achieve uniform contraction of mechanical and optical surfaces as the instrument cools to its operating temperature of about 40 K. NIRISS’s all-reflective design philosophy also mitigates against chromatic effects, which can be exacerbated by cryogenic conditions. Finally, some relevant properties of NIRISS NRM are described in the [Appendix](#).

2. BACKGROUND

(Figure 2) A non-redundant mask is a pupil plane mask typically located at a re-imaged pupil plane. It possesses several usually identical holes arranged so that no two hole-to-hole vectors are repeated (thus providing a non-redundant set of *baselines* in the pupil). If its holes are circular, with diameter d when projected back to the primary mirror, at a wavelength λ its point-spread function (PSF) or *interferogram* is contained in an Airy pattern envelope with a first dark ring of diameter $2.44 \lambda/d$ (Figure 1). This envelope is modulated by fringes with half period $\theta = \lambda/2B$ for each baseline. Here B is the hole

separation. Figure 2 shows the *JWST* NIRISS mask with seven hexagonal holes, and its PSF.

The Fourier transform of the detected in-focus two-dimensional image intensity array is the array of *complex visibility*, \mathcal{V} . Because of the baselines’ non-redundancy, the fringe amplitude and phase for each baseline or “two hole interferometer” component in the NRM can be measured unambiguously. The array of complex visibilities for a point source through unaberrated optics is the autocorrelation of the pupil mask. The resulting array of complex visibilities form localized *splodges* (Lloyd et al. 2006) of signal in the transform domain—conceptually one independent splodge (or a spodge and its dependent, Hermitian “mirror splodge”) per baseline. Numerical Fourier data analysis approaches measure fringe phases and fringe amplitudes, often at the peak of each splodge amplitude (Tuthill et al. 2000; Lloyd et al. 2006). When using a finite bandwidth filter, selecting a single amplitude and phase to characterize a polychromatic fringe implicitly averages over the bandpass. Furthermore, since windowing in the image plane leads to convolution in the Fourier domain, this induces a second form of averaging within a splodge. Our image plane approach avoids this second form of averaging, but it does perform a conceptually similar averaging over the bandpass. In the absence of wavefront aberration, fringe phases for an on-axis point source are zero. Information on source structure is contained in the fringes that are extracted from the image.

The non-redundancy of baselines in the pupil leads to constraints on the complex fringe visibilities. A *closure phase* (the cyclic sum of fringe phases around the baselines formed by three holes (top right, Figure 1)) is insensitive to constant wavefront delays (pistons) over the holes. The fringe formed by interference of holes i and j has a fringe phase $\phi_{i,j}$ which is proportional to the wavefront delay between holes $\phi_{i,j} \equiv \phi_j - \phi_i$. For a point source (in the absence of higher order aberrations) (e.g., Readhead et al. 1988):

$$\begin{aligned} \Delta\phi_{1,2} + \Delta\phi_{2,3} + \Delta\phi_{3,1} \\ = (\phi_1 - \phi_2) + (\phi_2 - \phi_3) + (\phi_3 - \phi_1) = 0. \end{aligned} \quad (1)$$

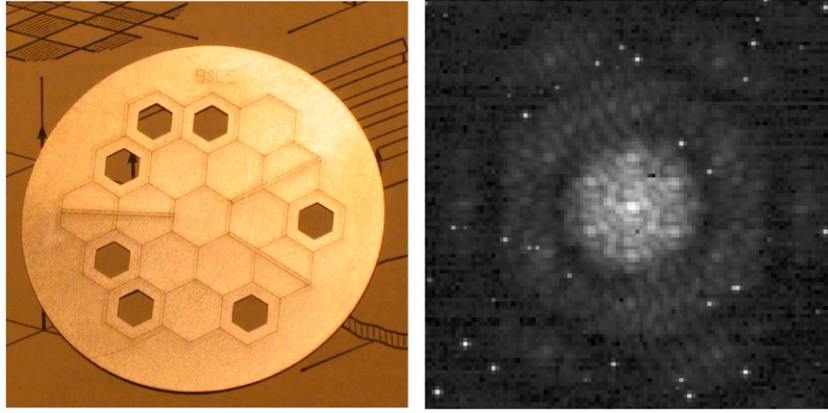


Figure 2. Non-redundant mask for *JWST*’s NIRISS pupil wheel (Sivaramakrishnan et al. 2010a) and its PSF (or interferogram) with NIRISS F430M from cryogenic vacuum tests in 2013 November (Greenbaum et al. 2014). The interferogram’s fine structure is due to the 21 baselines generated by the 7 holes. The PSF envelope reflects the hexagonal hole shape.

Full-aperture images do not yield closure phases, but sufficiently high Strehl ratio images possess certain constrained linear combinations of phases of the Fourier transform of the image (Martinache 2010, 2011). These combinations, or *kernel phases*, are useful for model fitting data when wavefront aberrations are below ~ 1 rad (Martinache 2010; Ireland 2013; Pope et al. 2013).

An N -hole mask has $N(N-1)/2$ baselines, $N(N-1)(N-2)/6$ closure phases, and $(N-1)(N-2)/2$ independent closure phases. Empirically, achievable dynamic range is approximately the inverse of the standard deviation of closure phase error, $1/\sigma_{CP}$ (Lacour et al. 2011).

Closure phases of centro-symmetric sky brightness distributions are zero. Binary or multiple point source models are fit to closure phase data to provide information on structure as fine as $\lambda/2B$. Instrumental contributions to closure phases are measured (in principle) by observing a point source. These contributions are then subtracted from a target’s closure phases. Instrument stability between target and calibrator leads to improved NRM performance. In addition to fringe phases, a space telescope is likely to provide stable fringe amplitudes. Closure amplitudes (a ratio of amplitudes of fringes formed by four holes (Thompson et al. 1986)) are useful in simple model fitting using space-based NRM data, thereby extending NRM model fitting to include centro-symmetric structure such as circular disks. However, Ford et al. (2014) use simulated noisy NIRISS NRM data to extract the fringe amplitudes and phases which they then use to recreate the input target scene with interferometric resolution. They found that enforcing closure quantities on image plane data leads to an increase in spurious image artifacts.

Currently numerical Fourier methods are the most common approach to NRM data analysis (e.g., Monnier 2003; Tuthill et al. 2000; Kraus & Ireland 2012; Ireland et al. 2008). This is suited to fields of view that encompass the first few Airy rings of the NRM PSF’s “primary beam” (the diffraction pattern of a single hole), and pixel scales that are significantly finer than $\lambda/2D$. Palomar Hale’s PHARO, Keck-NIRC2, and VLT’s NACO all possess 3-5 pixels per resolution element (Metchev & Hillenbrand 2004; Ireland et al. 2011; Tuthill et al. 2000; Girard 2013). With such super-Nyquist fine pixellation, Fourier methods easily identify and interpolate over isolated bad pixels (Ireland 2013).

Diffraction-limited exoplanet imagers deploying state-of-the-art ExAO systems now feed IFs (Oppenheimer et al. 2012; Macintosh et al. 2014; Beuzit et al. 2008). These imaging

spectrographs typically have limited fields of view since several detector pixels are required for each image plane pixel spectrum, and the angular extent of each image plane lenslet is at or below the diffraction limit of the telescope, so the instruments are often limited by the number of available detector pixels. NRM on these hyperspectral imagers—Palomar’s P1640 (Zimmerman 2011; Zimmerman et al. 2012) and Gemini Planet Imager (Sivaramakrishnan et al. 2010b; Greenbaum et al. 2013b)—must deal with this limitation. An image plane based approach (e.g., Lacour et al. 2011; Cheetham et al. 2012; Greenbaum et al. 2013a) is insensitive to these restrictions on the field of view.

Future space-based NRM on *JWST* NIRISS (e.g., Sivaramakrishnan et al. 2009a, 2009b, 2010a, 2012; Greenbaum et al. 2013a) is implemented on coarse pixel scales. Under these conditions a numerical Fourier data reduction approach may require more data in order to reduce contamination by bad pixels. This is more relevant to coarse—barely or sub-Nyquist—pixel scales. Dithering to fill the image plane pixels with valid data decreases observing efficiency and complicates estimates of noise. An image plane based approach sidesteps the requirement of knowing every pixel value in the image. The image plane approach is also robust to detector non-linearities that may occur at the centers of NRM images, since suspect pixel data can be discarded. *JWST* NIRISS’s coarse pixel scales also increase its sensitivity to non-uniform sensitivity within a pixel (intra-pixel sensitivity, or IPS), and pixel-to-pixel variations in IPS (Hardy et al. 2008). Image plane data reduction can take IPS into account, with a map of measured variations or a model of the pixel sensitivities (Greenbaum et al. 2013a).

3. IMAGE PLANE MODELING

We assume the image plane complex amplitude induced by a point source at infinity is described by the Fourier transform of the aperture transmission function (i.e., the Fraunhofer approximation). If functions F and f are a Fourier transform pair, we write $F \stackrel{F.T.}{\rightleftharpoons} f$. We develop a polychromatic image plane model tailored to *JWST* NIRISS’s seven hole NRM (Figure 2). Each hole is a hexagon, which, when projected to the *JWST* primary mirror, has a flat-to-flat distance of approximately 0.8 m. Our model can be adapted to arbitrary hole locations and polygonal hole shapes (e.g., Greenbaum et al. 2013b). Here we treat circular holes with diameter d or hexagonal holes with flat-to-flat distance D (Figure 3), utilizing a closed form for

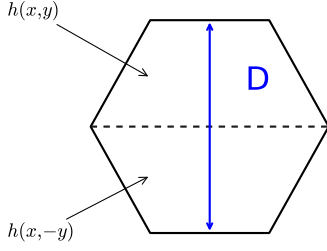


Figure 3. In Sabatke et al. (2005) D is the flat-to-flat distance. The hexagon is split into two symmetric parts, $a_{\text{hex}}(x, y)$ and $a_{\text{hex}}(x, -y)$, whose transforms, $g(k_x, k_y)$ and $g(k_x, -k_y)$ are computed analytically (Equation (6)).

the Fourier transform of a hexagon (Sabatke et al. 2005), while noting that other more specialized derivations for this exist in the literature (Troy & Chanan 2003). We extend the work of Sabatke et al. (2005) to include limiting values for the analytical expression's three singular lines and singular central point.

We calculate the monochromatic NRM PSF at a wavelength λ analytically, and construct polychromatic PSFs by summing appropriately weighted monochromatic PSFs on a finely sampled numerical grid. We then bin this finely sampled image to the detector pixel scale to simulate a pixelated noiseless NRM PSF.

We denote the pupil transmission function by $A(\mathbf{x})$. A hole with a transmission function $A_h(\mathbf{x})$ produces an image plane complex amplitude $a_h(\mathbf{k})$ (where $a_h \stackrel{F.T.}{\rightleftharpoons} A_h$) and a PSF $P = a_h a_h^*$ (where $*$ indicates complex conjugation). If the pupil plane vector $\mathbf{x} = (x, y)$ is in units of the wavelength of the monochromatic light, the image plane (or spatial frequency) vector $\mathbf{k} = (k_x, k_y)$ is in cycles across the pupil. $P(\mathbf{k})$ is the *primary beam*, by analogy with radio interferometry, and is the envelope of the NRM PSF. Vector baselines create the finer scale fringing in the NRM PSF.

3.1. Circular Mask Holes

A circular aperture's transmission function is

$$^2 \Pi(\mathbf{x}) = \begin{cases} 1, & r < \frac{1}{2} \\ 0, & r \geq \frac{1}{2} \end{cases}, \quad (2)$$

where $r = \sqrt{x^2 + y^2}$. The transmission function of a mask with N identical circular holes centered at $\{\mathbf{x}_i, i = 1, \dots, N\}$ is

$$A(\mathbf{x}) = \sum_{i=1}^N ^2 \Pi\left(\frac{\mathbf{x} - \mathbf{x}_i}{d_\lambda}\right), \quad (3)$$

(where $d_\lambda \equiv d/\lambda$). The image plane complex amplitude of an on-axis monochromatic point source observed through this mask is

$$a(\mathbf{k}) \stackrel{F.T.}{\rightleftharpoons} A(\mathbf{x}). \quad (4)$$

Following the nomenclature of phase retrieval work on the Hubble Space Telescope, we call $a(\mathbf{k})$ the *amplitude spread function* (ASF).

Invoking Fourier shift and scaling theorems,

$$^2 \Pi\left(\frac{\mathbf{x} - \mathbf{x}_0}{d_\lambda}\right) \stackrel{F.T.}{\rightleftharpoons} (d_\lambda)^2 \text{Jinc}(kd_\lambda) e^{-i\mathbf{k} \cdot \mathbf{x}_0}, \quad (5)$$

where $\text{Jinc}(k) \equiv J_1(\pi k)/2k$ is the transform of the circular transmission function. Here J_1 is the Bessel function of the first kind, of order 1. The phase gradient term $e^{-i\mathbf{k} \cdot \mathbf{x}_0}$ reflects the shift of the hole's origin to \mathbf{x}_0 .

3.2. Hexagonal Mask Holes

We denote the hexagonal hole Fourier transform by $a_{\text{hex}}(\mathbf{k})$. Following Sabatke et al. (2005), $g(k_x, k_y)$ is the Fourier transform of one half of a hexagon that is bisected from one corner to its diametrically opposite corner (Figure 3):

$$\begin{aligned} g(k_x, k_y) &= \frac{\exp\left[-i\pi D \left(\frac{2k_x}{\sqrt{3}} + k_y\right)\right]}{4\pi^2(k_x^3 - 3k_x k_y^3)} (\sqrt{3}k_x - 3k_y) \\ &\times \left(\left\{ \exp(i\pi D \sqrt{3}k_x) - \exp\left[i\pi D \left(\frac{4}{\sqrt{3}}k_x + k_y\right)\right] \right\} \right. \\ &\quad \left. + (\sqrt{3}k_x + 3k_y)[\exp(i\pi D k_x/\sqrt{3}) - \exp(i\pi D k_y)] \right) \\ a_{\text{hex}}(k_y, k_x) &= g(k_x, k_y) + g(k_x, -k_y). \end{aligned} \quad (6)$$

The function g has numerical singularities along three lines, $k_x = 0$ and $k_x = \pm\sqrt{3}k_y$. The limiting behavior along $k_x = 0$ and at the origin is

$$\begin{aligned} g(0, k_y) &= \frac{e^{-iD\pi k_y}}{2\sqrt{3}\pi^2 k_y^2} \\ &\times (-1 + iD\pi k_y + e^{iD\pi k_y} - 2iD\pi k_y e^{iD\pi k_y}) \end{aligned} \quad (7)$$

$$g(0, 0) = \frac{\sqrt{3}D^2}{4}. \quad (8)$$

Values along the other two lines can be found by invoking symmetry arguments, and replacement with the appropriate limiting value taken from the $k_x = 0$ line.

3.3. Interference between Holes

In the absence of wavefront error the ASF of a mask with N identical holes centered at $\{\mathbf{x}_i, i = 1, \dots, N\}$ is

$$\sum_{i=1}^N A(\mathbf{x} - \mathbf{x}_i) \stackrel{F.T.}{\rightleftharpoons} a(\mathbf{k}) = a_h(\mathbf{k}) \sum_{i=1}^N e^{-i\mathbf{k} \cdot \mathbf{x}_i} \quad (9)$$

($a_h(\mathbf{k})$ is a single hole ASF). The mask's point spread function is

$$p(\mathbf{k}) = a(\mathbf{k})a^*(\mathbf{k}) = P(\mathbf{k}) \sum_{i=1}^N \sum_{j=1}^N e^{-i\mathbf{k} \cdot (\mathbf{x}_i - \mathbf{x}_j)} \quad (10)$$

or

$$\begin{aligned} p(\mathbf{k}) &= P(\mathbf{k}) \{ N + e^{-i\mathbf{k} \cdot (\mathbf{x}_1 - \mathbf{x}_2)} + e^{i\mathbf{k} \cdot (\mathbf{x}_1 - \mathbf{x}_2)} \\ &\quad + e^{-i\mathbf{k} \cdot (\mathbf{x}_1 - \mathbf{x}_3)} + e^{i\mathbf{k} \cdot (\mathbf{x}_1 - \mathbf{x}_3)} + \dots \}, \end{aligned}$$

(which is real and nonnegative for any \mathbf{k}). The flux in this image is the two-dimensional integral $\int NP(\mathbf{k})d\mathbf{k}$, taken over

the entire \mathbf{k} plane. We rewrite the PSF as

$$p(\mathbf{k}) = P(\mathbf{k}) \left\{ N + \sum_{i < j} 2 \cos(\mathbf{k} \cdot (\mathbf{x}_i - \mathbf{x}_j)) \right\}, \quad (11)$$

which shows the separate roles the vector baselines and the primary beam play in the morphology of a point source's interferogram.

Wavefront errors $\{\phi_i, i = 1, \dots, N\}$ that are constant within each of the apertures decenter each fringe by $(\phi_i - \phi_j)$. Such errors are termed *pistons*. Pistons do not move the image centroid, since the intensity centroid is the mean of the phase gradient over the (uniformly illuminated) pupil forming an in-focus image (Teague 1982), and piston errors do not change the mean wavefront slope. A piston difference between two holes shifts the fringe away from the image centroid (or *pointing center*) by an angle, the *fringe phase*. A shift from one fringe maximum to the next is interpreted as an angle of 2π . Given *JWST* NIRISS' anticipated image quality during normal operations, we expect fringe phases of point source NRM images to lie well inside the half-open interval $(-\pi, \pi]$. This removes any technical difficulties associated with a fringe phase wrapping around 2π . We stress that fringe phases are not the argument of a “phasor” associated with the complex amplitude of an electromagnetic wave. The expression for the interferometric PSF in the presence of only piston errors is

$$\begin{aligned} p(\mathbf{k}) &= P(\mathbf{k}) \sum_{i=1}^N \sum_{j=1}^N e^{-i\mathbf{k} \cdot (\mathbf{x}_i - \mathbf{x}_j) + i(\phi_i - \phi_j)} \\ &= P(\mathbf{k}) \left\{ N + \sum_{i < j} 2 \cos(\mathbf{k} \cdot (\mathbf{x}_i - \mathbf{x}_j) + (\phi_i - \phi_j)) \right\} \\ &= P(\mathbf{k}) \left\{ N + \sum_{i < j} 2(\cos(\mathbf{k} \cdot (\mathbf{x}_i - \mathbf{x}_j)) \cos(\phi_i - \phi_j) \right. \\ &\quad \left. - \sin(\mathbf{k} \cdot (\mathbf{x}_i - \mathbf{x}_j)) \sin(\phi_i - \phi_j)) \right\}. \end{aligned} \quad (12)$$

3.4. The *JWST* NRM PSF

For *JWST* NIRISS's 7-hole hexagonal mask, Equation (12) gives

$$\begin{aligned} p(\mathbf{k}) &= P(\mathbf{k}) \{ 7 + 2 \cos(\mathbf{k} \cdot (\mathbf{x}_1 - \mathbf{x}_2)) \cos(\Delta\phi_{1,2}) \\ &\quad - 2 \sin(\mathbf{k} \cdot (\mathbf{x}_1 - \mathbf{x}_2)) \sin(\Delta\phi_{1,2}) \\ &\quad + 2 \cos(\mathbf{k} \cdot (\mathbf{x}_1 - \mathbf{x}_3)) \cos(\Delta\phi_{1,3}) \\ &\quad - 2 \sin(\mathbf{k} \cdot (\mathbf{x}_1 - \mathbf{x}_3)) \sin(\Delta\phi_{1,3}) + \dots \}. \end{aligned} \quad (13)$$

With this closed form rapid calculation of monochromatic and polychromatic PSFs on a fine scale is straightforward.

3.5. Linear Fit

Piston differences enter into Equation (13) as coefficients of the sines and cosines describing the baselines' fringes. NIRISS's seven-hole mask has 42 such fringe coefficients— $\cos\Delta\phi_{i,j}$'s and $\sin\Delta\phi_{i,j}$'s, which we rename a_{ij} 's and b_{ij} 's, respectively. Two additional parameters are required to match the model to data: the average flux per hole, F , and a DC offset C :

$$\begin{aligned} F P(\mathbf{k}) \left\{ N + \sum_{i < j} 2[\cos(\mathbf{k} \cdot (\mathbf{x}_i - \mathbf{x}_j)) \cos(\Delta\phi_{i,j}) \right. \\ \left. - \sin(\mathbf{k} \cdot (\mathbf{x}_i - \mathbf{x}_j)) \sin(\Delta\phi_{i,j})] \right\} + C. \end{aligned} \quad (14)$$

These 44 parameters can be estimated from image plane pixel data by using an unweighted *linear* least squares minimization of the quantity

$$||\text{data} - \text{model}(a_{ij}, b_{ij}, F, C)||$$

and performing a matrix inversion to recover the parameters. We did not detect significant improvement of a noise-weighted fit over an equally weighted fit, so we use the latter. The piston differences, or fringe phases, are found with

$$\Delta\phi_{ij} = \arctan(b_{ij}/a_{ij}). \quad (15)$$

For uniformly transmissive optics throughput, no scattered light, no significant high spatial frequency wavefront errors, and perfect detectors we expect the trigonometric identity

$$b_{ij}^2 + a_{ij}^2 = 1$$

to hold when imaging a point source. Model parameters derived from fitting real data rarely obey this identity. Instead, we obtain the square of the ij^{th} fringe visibility:

$$b_{ij}^2 + a_{ij}^2 = \mathcal{V}_{ij} \mathcal{V}_{ij}^*. \quad (16)$$

Target structure further reduces fringe visibility. We calculate fringe visibilities in our simulated data sets by measuring coefficients $\{a_{ij}, b_{ij}\}$. We calculate all 35 possible closure phases in NIRISS's seven-hole NRM. Only 15 of these are independent measurements.

We evaluate our model PSF on a 3×3 sub-pixel grid (unless otherwise noted) so we can study sub-pixel effects, and then bin the array to the detector pixel scale. A full pupil distortion model was not used in this study, although real data will require detailed knowledge of the NRM-to-primary mapping.

A polychromatic model is generated with an appropriately weighted sum of each monochromatic fringe model, given the bandpass profile:

$$\begin{aligned} \text{model} &= \sum_{\lambda} F_{\lambda} P(\mathbf{k}_{\lambda}) \\ &\times \left\{ N + \sum_{i < j} 2[\cos(\mathbf{k}_{\lambda} \cdot (\mathbf{x}_i - \mathbf{x}_j)) \cos(\Delta\phi_{i,j}) \right. \\ &\quad \left. - \sin(\mathbf{k}_{\lambda} \cdot (\mathbf{x}_i - \mathbf{x}_j)) \sin(\Delta\phi_{i,j})] \right\}. \end{aligned} \quad (17)$$

In the presence of non-zero piston error the model in Equation (14) does not fit polychromatic data perfectly, because piston error scales inversely with wavelength. This means that the fringes' coefficients, $\cos(\Delta\phi_{i,j})$ and $\sin(\Delta\phi_{i,j})$, themselves vary with wavelength, but our fit keeps these coefficients constant over the bandpass. The narrower the fractional bandwidth of the filter, the smaller the variation of these coefficients. This problem is common to both the image plane as well as the numerical Fourier approach to NRM data analysis. The least squares solution (Equations (15) and (16)) produces an estimate of fringe phase and amplitude that describes some average over the bandpass. We use this estimate in our polychromatic studies.

3.6. Applicability of the Model

NRM is suited to wavefronts that are smooth over each hole in the mask. Our model assumes flat wavefronts over each hole,